

Research Article

Research on Numerical Simulation of Tantalum Explosively Formed Projectile Forming Driven by Detonation

Yajun Wang ^{1,2}, Weibing Li ¹, Jiaxin Yu,¹ Wenbin Li,¹ and Heyang Xu¹

¹School of Mechanical Engineering, Nanjing University of Science and Technology, Nanjing 210094, China

²Xi'an Modern Control Technology Research Institute, Xi'an 710065, China

Correspondence should be addressed to Weibing Li; njustlwb@163.com

Received 15 March 2022; Revised 31 July 2022; Accepted 12 August 2022; Published 20 September 2022

Academic Editor: Hung Nguyen-Xuan

Copyright © 2022 Yajun Wang et al. This is an open access article distributed under the Creative Commons Attribution License, which permits unrestricted use, distribution, and reproduction in any medium, provided the original work is properly cited.

In order to study the formation characteristics of tantalum explosively formed projectile (EFP), based on LS-DYNA finite-element software, this article analyzes the influence of mesh size on tantalum EFP forming, compares the accuracy of JC constitutive parameters in different literature on the characterization of tantalum EFP forming, calculates the effective action time of detonation that drives EFP formation, and carries out experimental verification. The results show that the EFP forming velocity was less sensitive to grid size; however, the EFP shape was highly sensitive to grid size, among which the liner had the greatest influence. Besides, for the same density and different constitutive parameters, the velocity of the stabilized EFP was the same, but the change trend of velocity was different, which led to the difference in morphology. The verification test showed that a selection of appropriate JC constitutive parameters could simulate tantalum EFP forming. Finally, the effect of detonation products on EFP forming was reflected mainly in the axial acceleration and radial contraction of the tail skirt. The influence of explosives and detonation products on EFP forming can be ignored 80 μ s after the charge detonates. In this work, the numerical simulation method of tantalum EFP forming was studied, which provides guidance for the design and engineering application of tantalum EFP.

1. Introduction

An explosively formed projectile (EFP) is a projectile with a high speed and flight stability that is formed by an explosively driven liner. Developments of composite, depleted-uranium, and other new types of armor allow for constant enhancements in armor protection ability [1]. Traditional OFHC copper EFP is insufficient at causing fatal damage to armored targets. Because of its high density, high ductility, and other characteristics, tantalum has become one of the main liner materials and has become a hot issue in the research of shape-charge technology [2]. Fong and Kraft [3] studied the application of tantalum in EFP warheads, which confirmed the feasibility of tantalum as a liner material.

Rapid developments of numerical simulation technology have resulted in this convenient, intuitive, and efficient method gradually becoming the main means of EFP research. Numerical simulations of EFP, generally, using

hydrocodes such as LS-DYNA, ABAQUS, or AUTODYN, are used by analysts and scientists to gain valuable insight into the physics of these devices [4]. The accuracy of numerical simulation depends mainly on the calculation method, material model, and its parameters. More recently, Johnson and Stryk [5] explored issues related to modelling three-dimensional EFP, explaining the effects of the sliding/contact interfaces, the type and arrangement of elements, and the generation of the grid. Cardoso and Teixeira-Dias [6] discussed effects on behavior and performance of EFP parameters, and described a numerical simulation model to reproduce the conditions of formation and ballistic capabilities of EFP. Castedo et al. [4] show that 2D and 3D Lagrangian simulations of a nonindustrial copper and steel EFP are sufficient for simulating the whole EFP process. Mulligan and Jensen [7] focus on smoothed particle hydrodynamics (SPH) to describe and investigate physical characteristics of EFP, involving large deformation and

extremely high strain rates. Similar computational topics were extensively researched by Zhang and Jin [8], Wojewódka and Witkowski [9], Pappu and Murr [10], and Baêta-Neves and Ferreira [11], focusing on aspects such as the effect of meshing, blast load intensity, constitutive modelling, and the use of alternative methods. Research studies indicate that Lagrange, Arbitrary Lagrange Euler (ALE), and Lagrange/Euler hybrid methods are used mainly in the numerical simulation of EFP forming, whereas the Lagrange mesh is used to characterize the liner. In any case, they should be calibrated and validated with experimental (real) data for their results to be deemed reliable and useful. In the selection of a constitutive model, Johnson–Cook (JC), Zerilli–Armstrong (ZA), and Steinberg models are most commonly used to describe the plastic deformation characteristics of liner materials [12–14]. The plastic flow behavior of tantalum at a high temperature and a high strain rate has been given significant attention in recent decades. For the dynamic mechanical properties of tantalum, Chen and Gray [15] studied the stress-strain relationship of tantalum and analyzed its constitutive behavior. Kim et al. [16–20] carried out research and obtained the corresponding constitutive parameters. A series of test results showed that tantalum has a higher yield strength than OFHC copper and is sensitive to temperature. The choice of reliable constitutive parameters can improve the accuracy of the simulation results and guide practice.

For numerical simulation of the forming process of tantalum EFP, Wang et al. [21] discussed the influence of the matching relationship between a liner structure and a material on EFP forming characteristics, and the suitable liner structure types for tantalum EFP forming. Guo et al. [22] and Zhu et al. [23] discussed the influence of the tantalum liner structure parameters on EFP forming and penetration performance. Li et al. [24] analyzed the liner structure parameters to form tantalum tail EFP. In terms of initiation mode, Kumar et al. [25] discussed the influence of single-point initiation and circumferential multipoint initiation on the formation of tantalum EFP. Ding et al. [26] simulated the forming characteristics of tantalum EFP to analyze the axial fracture characteristics. However, most of the available literature on numerical methods mainly based traditional materials such as copper, ignored special analysis, and verification for tantalum. What's more, the influence of detonation driving time on tantalum EFP forming, the detailed numerical simulation method, and real tests used to support the simulation have generally been overlooked.

To study the forming characteristics of tantalum EFP, based on LS-DYNA finite-element software, this article analyzes the influence of mesh size on tantalum EFP forming, compares the accuracy of JC constitutive parameters in different literature on the characterization of tantalum EFP forming, calculates the effective action time of detonation that drives EFP formation, and carries out experimental verification. In this work, the numerical simulation method of tantalum EFP forming was studied, which provides guidance for the design and engineering application of tantalum EFP.

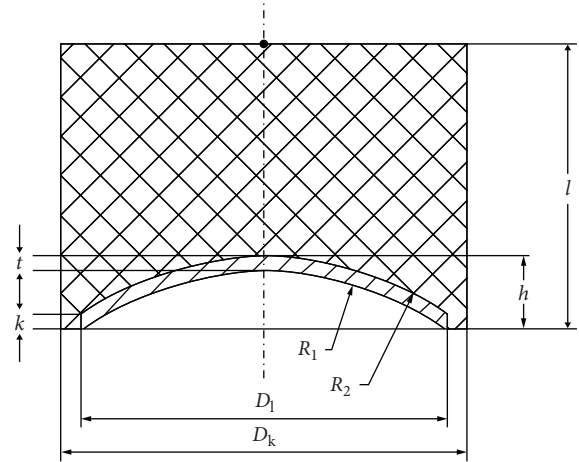


FIGURE 1: Schematic diagram of shaped charge structure.

2. Numerical Simulation Model

2.1. Warhead Structure. The structure and size of the liner are important to form an explosively formed projectile. With an increase in liner cone angle or a decrease in liner top height, the jet and pestle body tend to the same velocity and become indistinguishable, which yields a forming EFP. In this article, based on the tulip liner, the charge diameter D_K is 70 mm, and the charge structure is designed as shown in Figure 1.

The charge diameter D_K was 70 mm, the charge height L was $0.7 D_K$, and the single-point initiation was used at the bottom center of the charge. The liner adopts an eccentric subhemisphere structure. The diameter of the liner was 63 mm ($0.9 D_K$). The inner and outer radii of liners R_1 and R_2 were 64.86 mm, and the thickness at the center and the edge t and k was 2.52 mm.

2.2. Establishment of Simulation Model. The finite-element calculation model was composed of an explosive, liner, and air. As shown in Figure 2, the element type is a 164 element (8-node hexahedral solid element). Because the warhead model is a symmetrical structure, based on the initiation mode and calculation time, half of the structure was selected to establish a three-dimensional model. When building a half finite-element model, it is necessary to impose symmetry constraints on the symmetry planes, that is, to constrain the displacement and rotation degrees of the freedom of the nodes on these symmetry planes.

The forming process of the tantalum liner EFP was simulated by ANSYS/LS-DYNA software. The ALE algorithm was used in the simulation. The explosive and air were divided into Euler grids, whereas the liner was divided into Lagrange grids and placed in the Euler grids. The fluid/structure coupling method was used between the Euler and Lagrange grids. To avoid the reflection of pressure on the boundary and to eliminate the boundary effect, the non-reflecting boundary condition was applied on the boundary nodes in the air computational domain. During the calculation, the hourglass was easy to produce by single-point

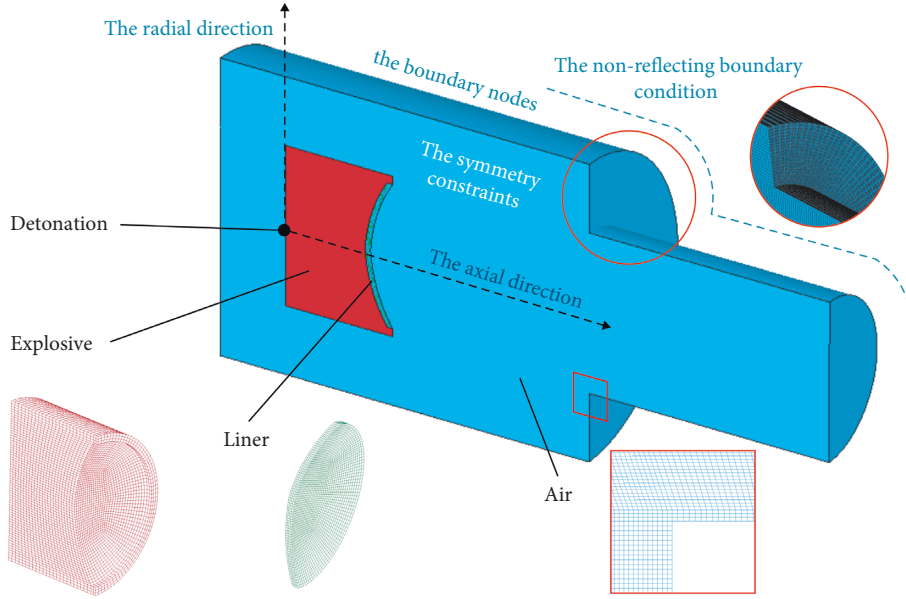


FIGURE 2: Simulation calculation model.

integration, and numerical oscillation occurred, so hourglass control was used.

2.3. Material Parameters. The main charge was a JH-2 high explosive, which is described by the high-explosive-burn material model and JWL state equation. The JWL state equation can describe the pressure, volume, and energy characteristics of the explosive detonation products during expansion and driving. Equation (1) is used extensively and is a reasonable equation of state for explosive detonation. Its specific expression form is

$$p = A \left(1 - \frac{\omega}{R_1 \bar{V}} \right) \exp(-R_1 \bar{V}) + B \left(1 - \frac{\omega}{R_2 \bar{V}} \right) \exp(-R_2 \bar{V}) + \frac{\omega E}{\bar{V}}, \quad (1)$$

where A , B , R_1 , R_2 , and ω are constants, \bar{V} is the relative specific volume of detonation products, and E is the internal energy per unit volume of explosive.

The null material model and linear polynomial state equation were selected to describe the air, which is given as

$$p = C_0 + C_1 \mu + C_2 \mu^2 + C_3 \mu^3 + (C_4 + C_5 \mu + C_6 \mu^2) E, \quad (2)$$

where p is pressure, E is internal energy, and C_0 , C_1 , C_2 , C_3 , C_4 , C_5 , and C_6 are polynomial equation coefficient. And $\mu = \rho/\rho_0 - 1$, ρ/ρ_0 is the ratio of current density to reference density. ρ_0 is a nominal or reference density. If $\mu < 0$, where terms $C_2 \mu^2 = 0$, $C_6 \mu^2 = 0$.

The liner material was tantalum and was described by the JC constitutive model and the Grüneisen equation of state. The JC constitutive model reflects the relationship between the plastic rheological behavior of materials and the strain rate, temperature, and strain-strengthening effect. The model has high reliability and is used extensively to describe

the plastic deformation behavior of various metal materials at a large strain, high strain rate, and high temperature:

$$\sigma = (A + B \varepsilon_p^*) (1 + C \ln \varepsilon_p^*) (1 - T^{*m}), \quad (3)$$

where σ is the von Mises equivalent stress; A is the yield stress, B is the strain hardening coefficient, C is the strain rate correlation coefficient, n is the strain hardening exponent, and n and m are constants. ε_p is the equivalent plastic strain, and ε_p^* is the dimensionless plasticity ratio. $T^* = (T - T_{\text{room}})/(T_{\text{melt}} - T_{\text{room}})$ is the dimensionless temperature, where T is the absolute temperature, T_{room} is the room temperature, and T_{melt} is the melting temperature.

The Grüneisen equation of state defines the relationship between the material volume and pressure. For compressed materials, the expression of the Grüneisen equation of state is

$$p = \frac{\rho_0 C^2 \mu [1 + (1 - (\gamma_0/2))\mu - (a/2)\mu^2]}{[1 - (S_4 - S)\mu - S_2(\mu^2/(\mu + 1)) - S_3(\mu^3/(\mu + 1)^2)]^2} + (\gamma_0 + a\mu)E. \quad (4)$$

For expansive materials, the equation is characterized as

$$p = \rho_0 C^2 \mu + (\gamma_0 + a\mu)E, \quad (5)$$

where C is the sound speed of the static body of the material; S_1 , S_2 , and S_3 are the coefficients that determine the shape of $v_s - v_p$ curve (Hugoniot line); and γ_0 is the Grüneisen gamma; $\mu = (\rho - \rho_0)/\rho_0$, where ρ_0 is the initial density and ρ is the current density; a is the first order volume correction to γ_0 ; E is the internal energy of initial unit volume material. In the calculation, data from reference [20] are used in the

TABLE 1: Parameters of each material model in numerical simulation [27, 28].

JH-2	$\rho/(\text{g}\cdot\text{cm}^{-3})$	$D/(\text{m}\cdot\text{s}^{-1})$	$P_{C1}/(\text{GPa})$	$A/(\text{GPa})$	$B/(\text{GPa})$	R_1	R_2	ω	$E_0/(\text{GPa})$	V_0
	1.701	8212	29.6	854.5	20.493	4.6	1.35	0.25	10.0	1.0
Tantalum	$\rho/(\text{g}\cdot\text{cm}^{-3})$	$G/(\text{GPa})$	$C/(\text{m}\cdot\text{s}^{-1})$	S_1	S_2	S_3	γ_0	a	$E_0/(\text{GPa})$	V_0
	16.69	69.9	3414	1.2	0	0	1.6	0.0	0.0	1.0
Air	$\rho/(\text{g}\cdot\text{cm}^{-3})$		C_1	C_2	C_3	C_4	C_5	C_6	$E_0/(\text{GPa})$	V_0
	0.001293		0	0	0	0.4	0.4	0	0.00025	1.0

grid analysis as constitutive parameters of tantalum, and other material parameters are shown in Table 1.

3. Analysis of Mesh Size Effect

Before the numerical simulation of explosion shock wave, the convergence analysis should be carried out to determine the acceptable grid size. In numerical simulation, accurate results can only be obtained by using the grid of this size or smaller.

EFP forming parameters mainly include forming velocity (v) and length diameter ratio (L/D). However, in order to describe EFP forming characteristics in more detail, starting from EFP forming velocity and forming shape characteristics, EFP forming velocity (v), projectile length (L), length of solid (L_s), diameter of tail skirt (D_t), and diameter of solid (D_s) are selected to analyze the EFP forming state [9], as shown in Figure 3.

3.1. Relationship between Mesh Size and Computing Time. In the numerical simulation, refining the model grid as much as possible can improve the calculation accuracy. Meanwhile, it is necessary to control the grid size to avoid a reduction in calculation time step because of the small grid size, to reduce the calculation efficiency and increase the computer hardware level requirement. To provide a reference to select the model mesh size, the calculation time for different grid schemes is counted with dual-core calculation by controlling the calculation conditions. For ease of comparison of the effect of mesh sizes, the grid size of liner is independent of charge and air, and each is a uniform grid. In addition, the action time of the explosives and detonation products on EFP forming is limited and so these units were deleted, such as explosives and air, to reduce the calculation time. A full restart was used to continue the calculation to $400\ \mu\text{s}$. The relationships between the grid size and grid number and computing time are shown in Figure 4. The ASUS work station has 16G RAM, which CPU is Intel (R) Core (IM) i7-3770.

As shown in Figure 4, the grid number of the calculation model depends mainly on the Euler element that is composed of charge and air. As the grid size of the model decreases from 3 mm to 1 mm, the grid number increases exponentially from 75 690 to 1 728 900, which is an increase of ~ 23 times. Therefore, the computing time of the model increases from 8 min to 794 min, which is ~ 100 times larger. The grid number is provided mainly by the Euler element that is composed of charge and air, which can be deleted after a certain time. Therefore, it is necessary to analyze the sensitivity of the grid size and convergence of the grids to

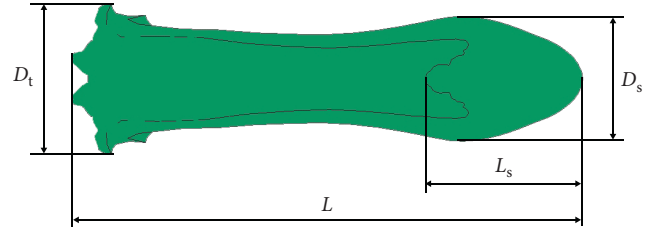


FIGURE 3: Schematic diagram of forming performance index of tantalum EFP.

improve the calculation efficiency to meet the calculation accuracy.

3.2. Influence of Mesh Size on EFP Formation Velocity. By using the numerical calculation model that was established in the previous section, the charge and air mesh that were based on the Euler element are consistent, and the liner that is based on the Lagrange element is divided separately. The EFP forming process of the tantalum liner was simulated numerically with grid sizes of 1, 1.5, 2, and 3 mm. The sensitivity of the forming tip and tail velocity of the EFP at $400\ \mu\text{s}$ to the grid size was obtained and is shown in Figure 5.

As shown in Figure 5, the shadow is the error band (velocity error of $\pm 3\%$). A decrease in the grid size results in a gradual velocity concentration where the grid size of the liner, charge, and air is 1 mm. With a decrease in charge and air grid, the liner size was concentrated from 1 to 2 mm, but the 3-mm liner showed no obvious change. The influence of the grid size of the charge and air was limited. The EFP forming velocity was less sensitive to the grid size. Besides the liner size, the charge and air grid were all 3 mm.

3.3. Influence of Grid Size on EFP Shape. For a change in EFP morphology, the curve of the EFP forming parameters at $400\ \mu\text{s}$ for different grid conditions was obtained and is shown in Figure 6.

As shown in Figure 6, an excessive mesh size leads to serious EFP shape distortion. The EFP shape is highly sensitive to mesh size. An increase in mesh density tends to result in the same shape parameters of the EFP. When the grid size of the charge and air was 1.5 mm, the liner size was less than or equal to 1.5 mm. When the grid size of charge and air was 1 mm, the liner size was less than or equal to 2 mm. The calculation was convergent. Compared with the molding velocity, when the size of the liner grid was 3 mm, the molding shape was distorted. The difference is that the shape was affected by the grid size of the charge and air. To analyze the sensitivity of the EFP forming shape to the air

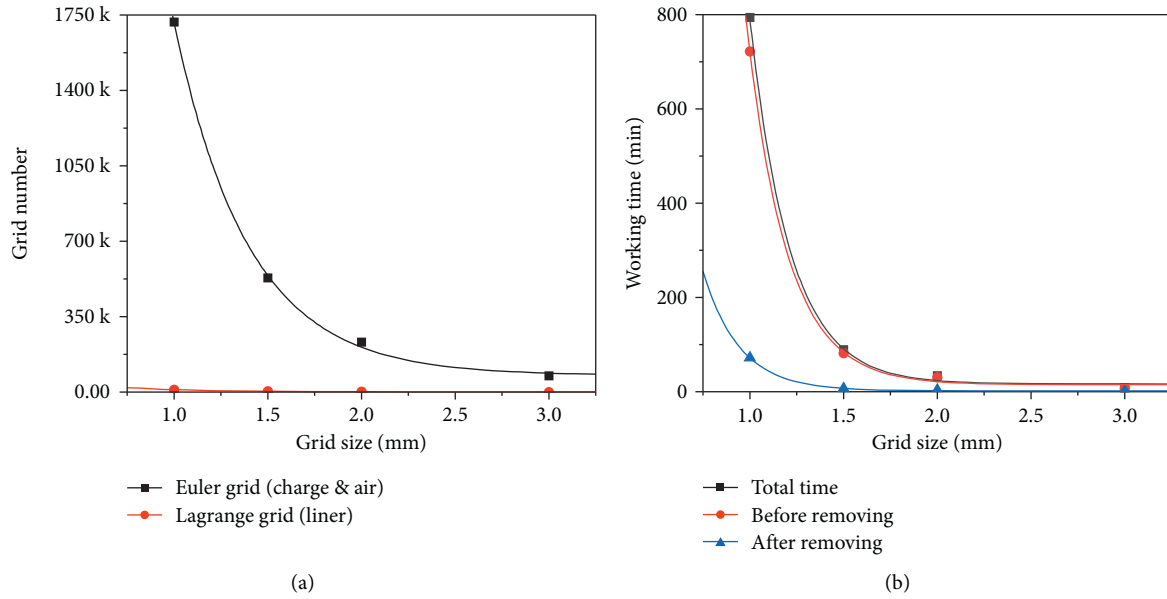


FIGURE 4: Curve of grid numbers and computing time versus grid size. (a) Grid number. (b) Computing time.

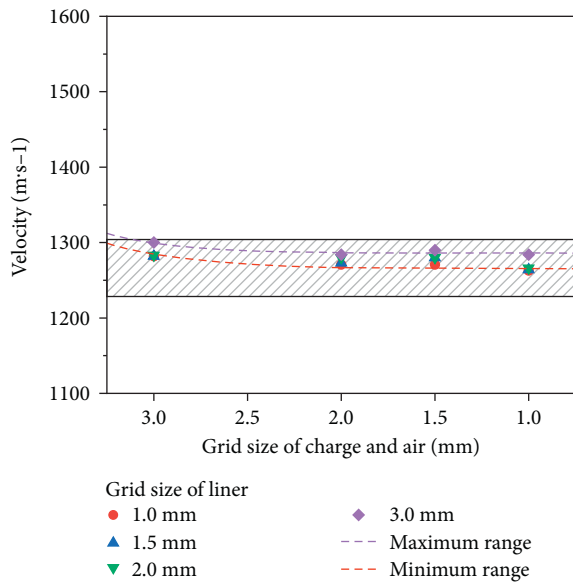


FIGURE 5: Velocity curve of EFP forming tip and tail.

grid size, the grid size of the charge and liner was controlled to 1 mm, and the variation curves of the EFP forming characteristic parameters for different air grid sizes were obtained, as shown in Figure 7.

As shown in Figure 7, compared with a simultaneous change in charge and air grid, the overall variation range of characteristic parameters is small when the air grid size is adjusted separately, and the distortion is not obvious when the air grid size is 3 mm. The EFP shape is more sensitive to the liner grid size, but is less sensitive to the air grid size. According to the statistical results, when the air grid size increased from 1 to 3 mm, the grid number decreased by 579 156. Even for an increase to 2 mm, the grid number decreased by 453798, which is more than half of the original

grid number. Therefore, in the mesh generation, it is necessary to ensure the mesh quality of the liner, select the appropriate charge grid size, and increase the grid size of air to improve the calculation efficiency.

In summary, in the grid generation, it is reasonable to set up the axial dimension of the liner mesh at 0.5 mm and the radial dimension at 1 mm; 1.5 mm in the axial direction and 1 mm in the radial direction for the charge; to divide the air gradient with a gradual increase, with an axial direction of 1.5, 2, and 3 mm, and a radial direction of 1 and 2 mm. For the numerical simulation model in this section, the number of grids of the liner is 7776, the total number of charge and air is 382 710, and the computing time is controlled within 90 min.

4. Influence of Constitutive Parameters of Liner

4.1. Selection of Constitutive Parameters. The tantalum liner collapsed and overturned under the impact of an explosion to form an EFP. The tantalum material properties exert an important influence in this process. The choice of reliable constitutive parameters can improve the accuracy of the simulation results and guide practice. The JC constitutive model has been applied extensively in the characterization of a variety of materials with a high accuracy. To analyze whether the JC constitutive model is suitable for tantalum EFP numerical simulations, this work summarizes the JC constitutive parameters that have been published and carries out numerical simulation calculations to discuss its applicability. The specific JC constitutive parameters are shown in Table 2. Some data in Table 2 are not provided in the original literature, and the data in brackets are guesses.

As shown in Table 2, many sets of JC constitutive characteristic parameters of tantalum have been reported. To analyze the description of each parameter on the stress-strain relationship of tantalum, based on the above

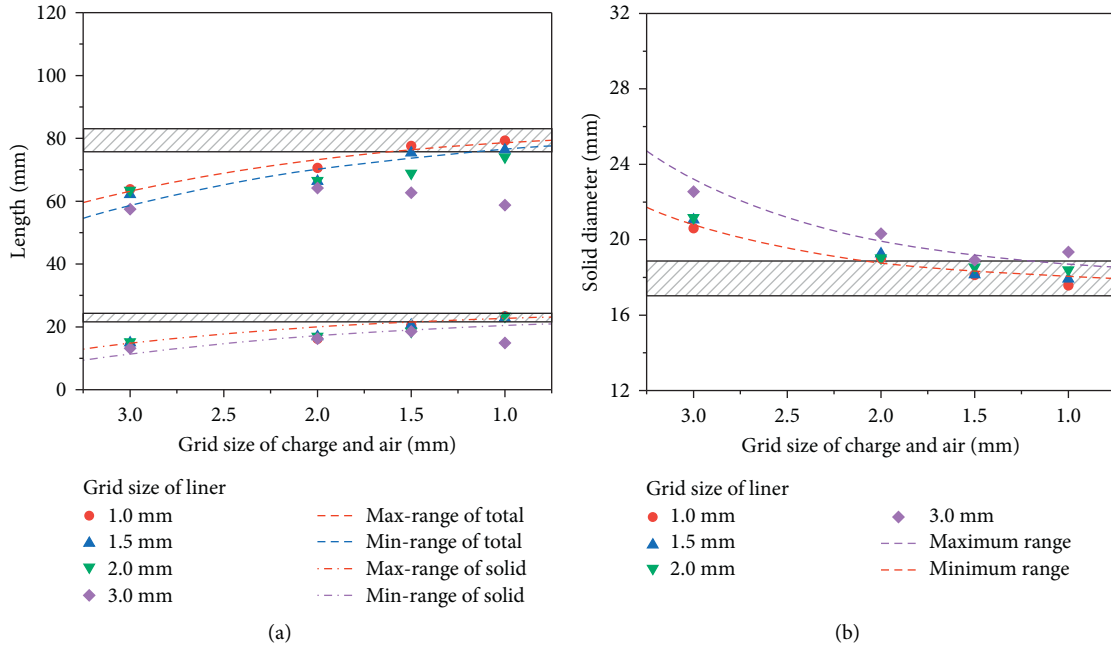


FIGURE 6: Variation curve of shape characteristic parameters of EFP. (a) Length and length of solid. (b) Diameter of solid.

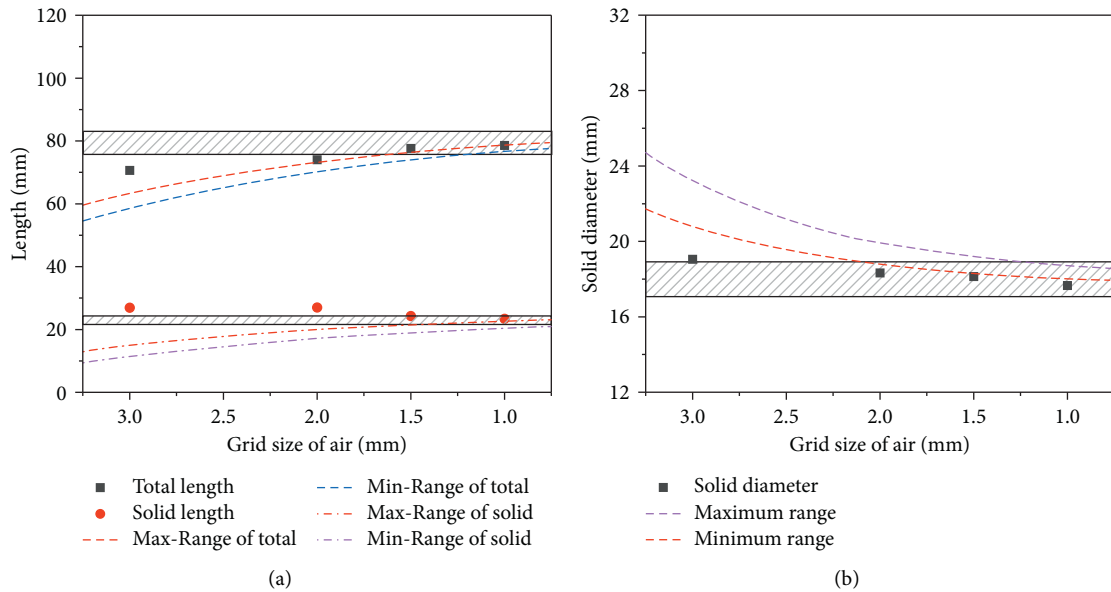


FIGURE 7: Variation curve of EFP shape characteristic parameters with air grid. (a) Length and length of solid. (b) Diameter of solid.

constitutive parameters, stress-strain curves of tantalum at different strain rates and temperatures were produced, as shown in Figure 8.

As shown in Figure 8, each constitutive parameter shows the same trend to characterize the stress-strain relationship of tantalum, but the specific values differ. Under the quasi-static condition (0.001/s), the characterization shows a certain degree of discrimination, and the values of parameters 4 and 8 are low and 4 was too low to be shown. With an increase in temperature, the difference between the values was reduced, and the softening effect of 6 was less obvious.

Under the dynamic condition (7000/s), the difference in parameter characterization was less obvious than that under the quasi-static condition, and the increase in stress with the increase in strain of 2 was more obvious. At a high temperature, 6 and 8 were higher; 4, 5, 7, and 9 were lower, whereas 1 and 3 existed between the two. The stress of parameter 2 increased significantly with an increase in strain, which was different from the actual situation. Parameters 4 and 8 were weak in describing the quasi-static or low strain rate conditions. Other parameters need to be judged according to the numerical simulation results.

TABLE 2: JC constitutive characteristic parameters of tantalum.

Number	A (MPa)	B (MPa)	n	C	m	Tm (K)	Tr (K)	$\dot{\epsilon}$	Reference
1	220	520	0.325	0.0550	0.475	3250	298	10^{-3}	[15]
2	340	750	0.7	0.0575	0.4	3250	298	10^{-3}	[15]
3	185	675	0.300	0.0470	0.425	3250	298	10^{-3}	[15]
4	800	550	0.4	0.0575	0.44	3293	(298)	(10^7)	[10]
5	611	704	0.608	0.015	0.251	3250	(298)	10^7	[16]
6	342.4	263.5	0.3148	0.057	0.8836	3269	298	4×10^{-4}	[17]
7	204	147	0.8	0.093	0.4	3123	296	10^{-4}	[18]
8	410	410	0.2	0.1	0.6	3269	298	10	[19]
9	187	267	0.38	0.054	0.45	3269	298	10^{-3}	[20]

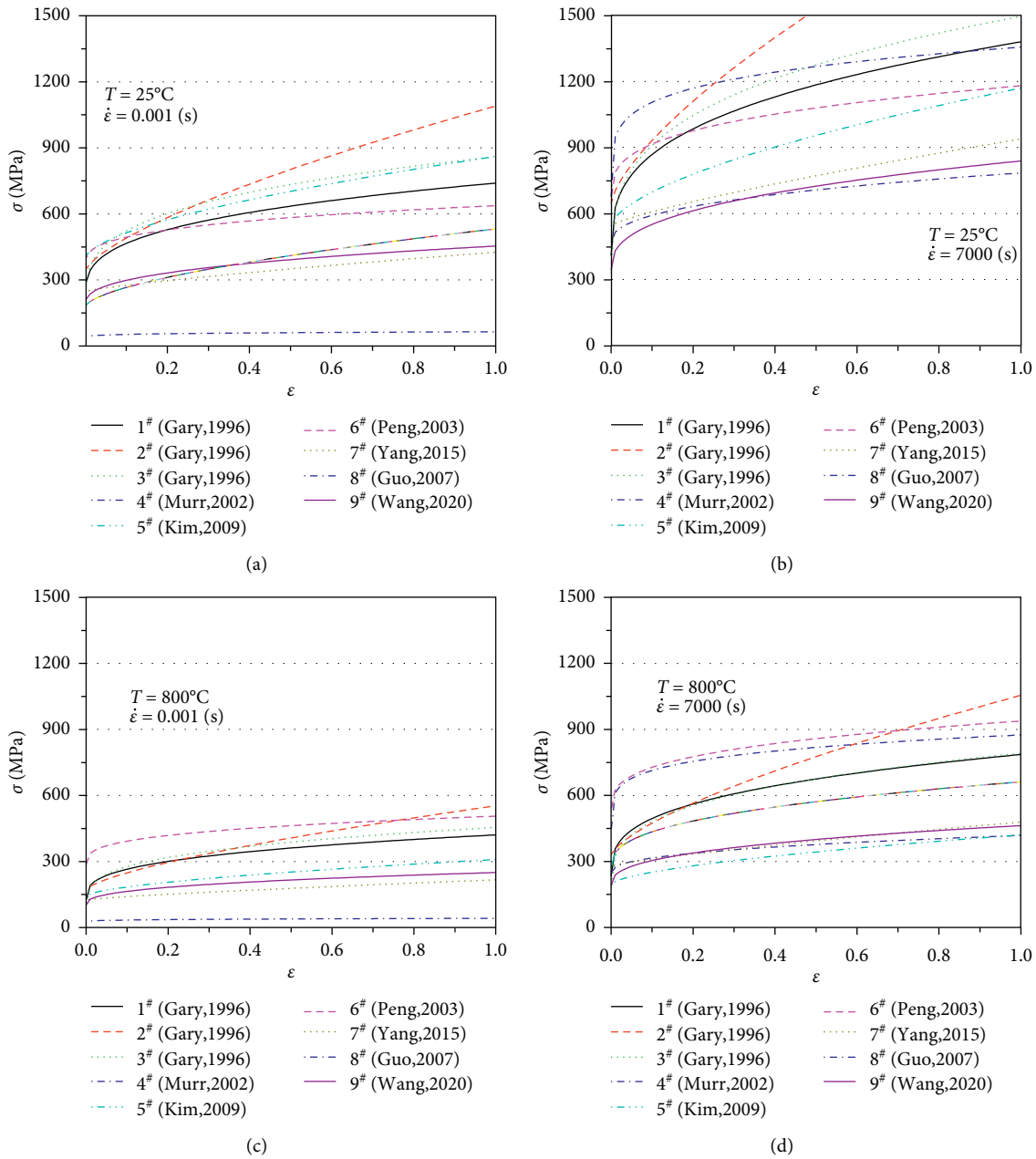


FIGURE 8: Stress-strain relationship of tantalum under different JC parameters. (a) Strain rate is 0.001/s at room temperature. (b) Strain rate is 7000/s at room temperature. (c) Strain rate is 7000/s at high temperature. (d) Strain rate is 0.001/s at high temperature.

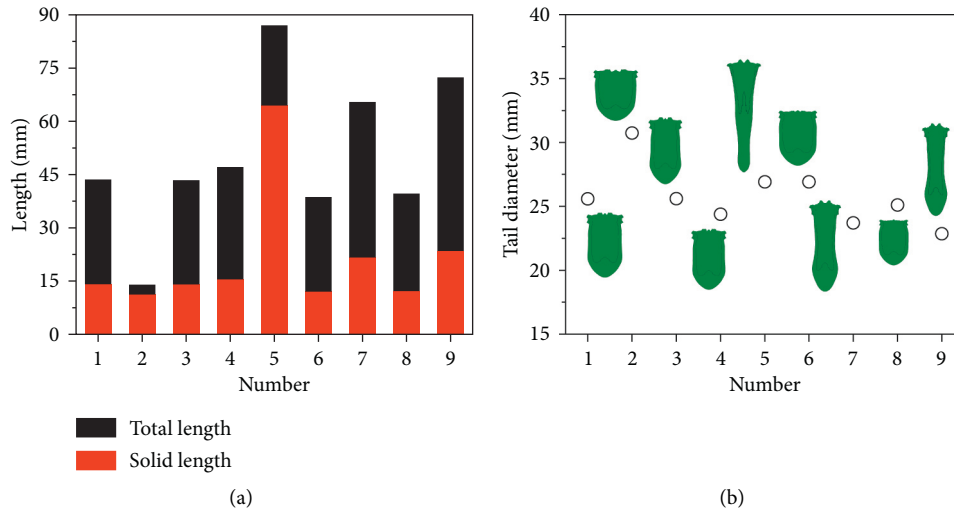


FIGURE 9: EFP shape characteristic parameters under different JC parameters. (a) Length and length of solid. (b) Tail skirt diameter and shape.

4.2. Analysis of Simulation Results. Based on the above constitutive parameters, the structural model and numerical calculation method that was established in the previous section were used to carry out the numerical simulation, and the forming characteristic parameters of the tantalum EFP under various parameters were obtained. At $400 \mu\text{s}$ after charge initiation, the flight velocity of the tantalum EFP was the same at 1275 m/s . The shape and characteristic parameters of the tantalum EFP are shown in Figure 9. Because some EFPs did not form a complete dense part, only the tail skirt diameter was included for the convenience of comparison.

As shown in Figure 8, the morphology of the tantalum EFP for different constitutive parameters is different. Among them, the length of the EFP that was formed by 2 was the smallest, because of the significant increase in stress with the increase in strain, which makes it difficult to extend the EFP. The length of the EFP that was formed by 5 was the largest, most likely because of the low strain rate and temperature softening effect in each parameter. The EFP forming mode of each parameter under the structure is a combination of center crushing and overall overturning, which forms the projectile with the same tip and tail velocity. The difference exists in the crushing degree and tensile length. The forming states of 1, 2, 3, 4, 6, and 8 were similar; 6 and 9 were similar, whereas 5 was different from the others and the crushing effect was obvious. According to the calculation results, the stable velocity of each scheme after EFP forming was the same at 1275 m/s . The forming velocity change curve of each scheme is shown in Figure 10. For the convenience of observation, the nine parameter schemes were divided into two groups. Parameters 1, 2, 3, 4, 6, and 8 were placed into the first group, and 2, 5, 7, and 9 were placed into the second group.

As shown in Figure 10, although the velocity of each part of the EFP after stabilization was the same for different parameters, the velocity change trend was different. For parameters 1, 2, 3, 4, 6, and 8, which were similar in overall

shape and velocity trend, the specific values were different, which led to slight differences in shape. The velocity of each part was the fastest to reach agreement when the total length and the length of the compaction part were shortest under scheme 2. The length under scheme 4 was relatively long, and its complete molding time was the latest. Because the velocity change trend differed from other schemes, the EFP that was formed by scheme 5 showed the most obvious shape difference, which reflected the difference in crushing, overturning and stretching of the liner under the stress-strain relationship. Different stress-strain relationships led to different action processes of the liner under explosive and detonation products, and they formed different EFP shapes. The final stable velocity of the EFP was unaffected by the material stress-strain relationship, and depended only on the material density or liner quality.

4.3. Experimental Verification. The test was carried out with the same shaped charge structure as the simulation calculation. The charge was pressed by a JH-2 explosive with a density $\rho_0 = 1.70 \text{ g/cm}^3$, as shown in Figure 11.

Pulse X-ray photography was used to photograph the molding form of tantalum EFP, as shown in Figure 12. The test system used a 450-kV pulse X-ray photography system (Scandiflash, Sweden) with two X-ray tubes arranged at 45° . The shaped charge specimen was placed vertically on the high explosive cylinder to ensure that the shaped penetrator passed through the intersection axis of the two X-ray tubes. Two X-ray tubes were set with different light output times to obtain X-ray photographs at different times, which corresponds to the tantalum EFP shape at 150 and $230 \mu\text{s}$. The obtained X-ray photographs were compared with the EFP shape and characteristic parameters that were obtained by finite-element software simulation under the same conditions.

By measuring the shape and displacement of the EFP and by considering the magnification in the X-ray photography

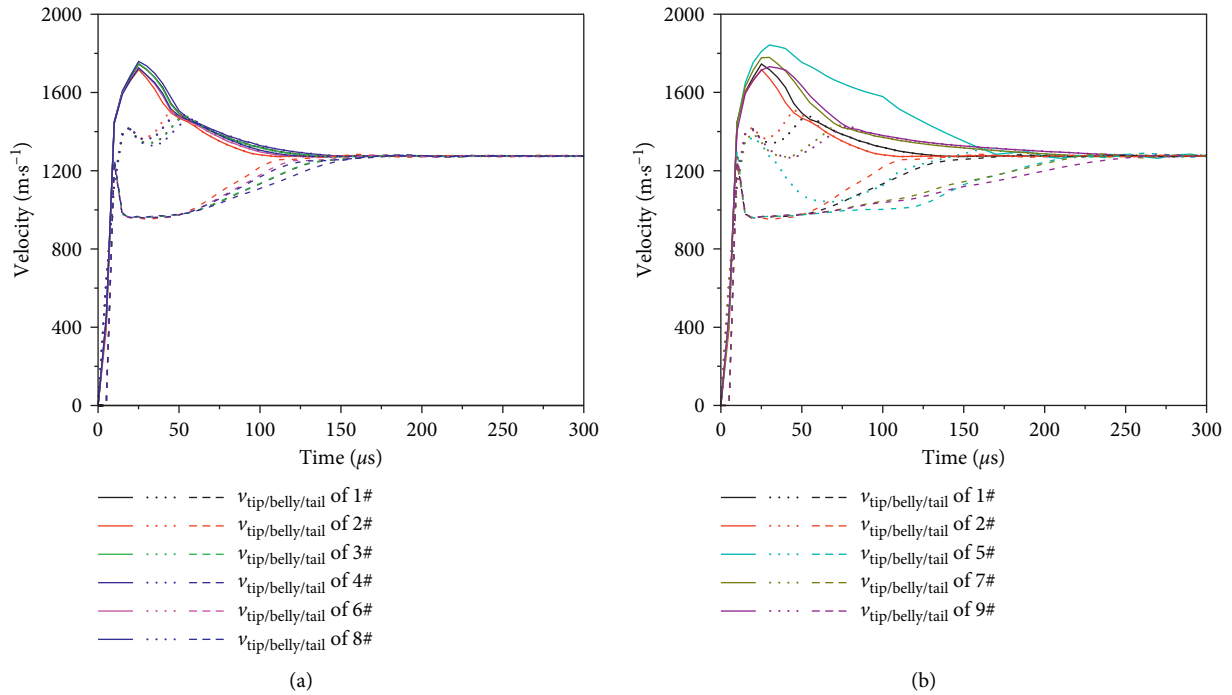


FIGURE 10: Tip/middle/tail velocity curves of EFP with different JC parameters. (a) 1#, 2#, 3#, 4#, 6#, 8#. (b) 1#, 2#, 5#, 7#, 9#.

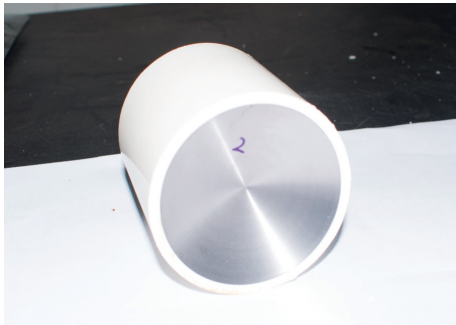


FIGURE 11: Shaped charge with tantalum liner for the test.

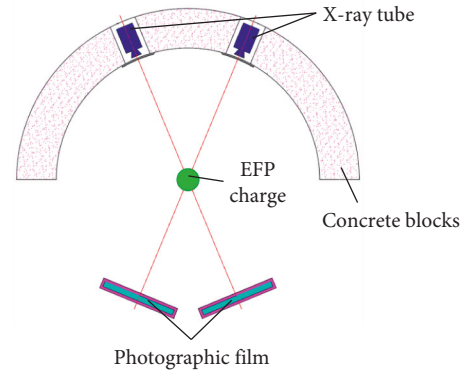


FIGURE 12: Layout diagram of the pulse X-ray test.

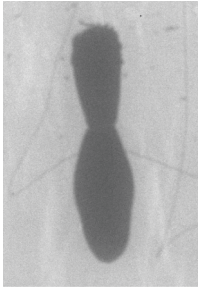
experiment, the velocity of the EFP was 1254 m/s, and the error between the test and simulation results (1275 m/s) was less than 2%. According to the experimental results, the ratio of length to diameter (L/D) of the EFP at $230 \mu s$ was 3.93, which was compared with the numerical simulation results, as shown in Table 3.

As shown in Table 3, the EFP formed for different constitutive parameters can be divided into three types. The EFPs that were formed by 1, 2, 3, 4, 6, and 8 had a smaller aspect ratio. The EFPs that were formed by 5 had a significant difference in the crushing mode compared with the test. The EFPs that formed by 7 and 9 agree better with the experimental results, and the error of 9 was less than 1%. Compared with the EFP shape, the shape of 7 and 9 was closer to the experimental results. The formation of tantalum EFP can be simulated by selecting appropriate JC constitutive parameters.

5. EFP Forming Time Driven by Detonation Products

The ALE method is an extension of the Lagrange algorithm, which overcomes the shortcomings of the Lagrange and Euler descriptions, makes the computational grid no longer fixed and unattached to the fluid particles, and allows arbitrary movement relative to the coordinate system, so the accuracy of the EFP forming is higher. With an increase in calculation time, the time step decreases, and the overall calculation time increases significantly. However, the action time of the explosives and detonation products on EFP forming is limited [29]. In order to reduce the simulation calculation time and improve the efficiency, it is necessary to analyze the effective action time of detonation products on EFP forming, so as to facilitate the full restart setting.

TABLE 3: Comparison of test and simulation results ($230 \mu\text{s}$).

	X-ray experiment	Simulation								
		1#	2#	3#	4#	5#	6#	7#	8#	9#
Shape										
L/D	3.93	1.90	1.44	1.88	2.12	6.25	1.64	3.38	1.68	3.90
Error	—	51.7%	63.4%	52.2%	46.1%	59.0%	58.3%	14.0%	57.3%	0.76%

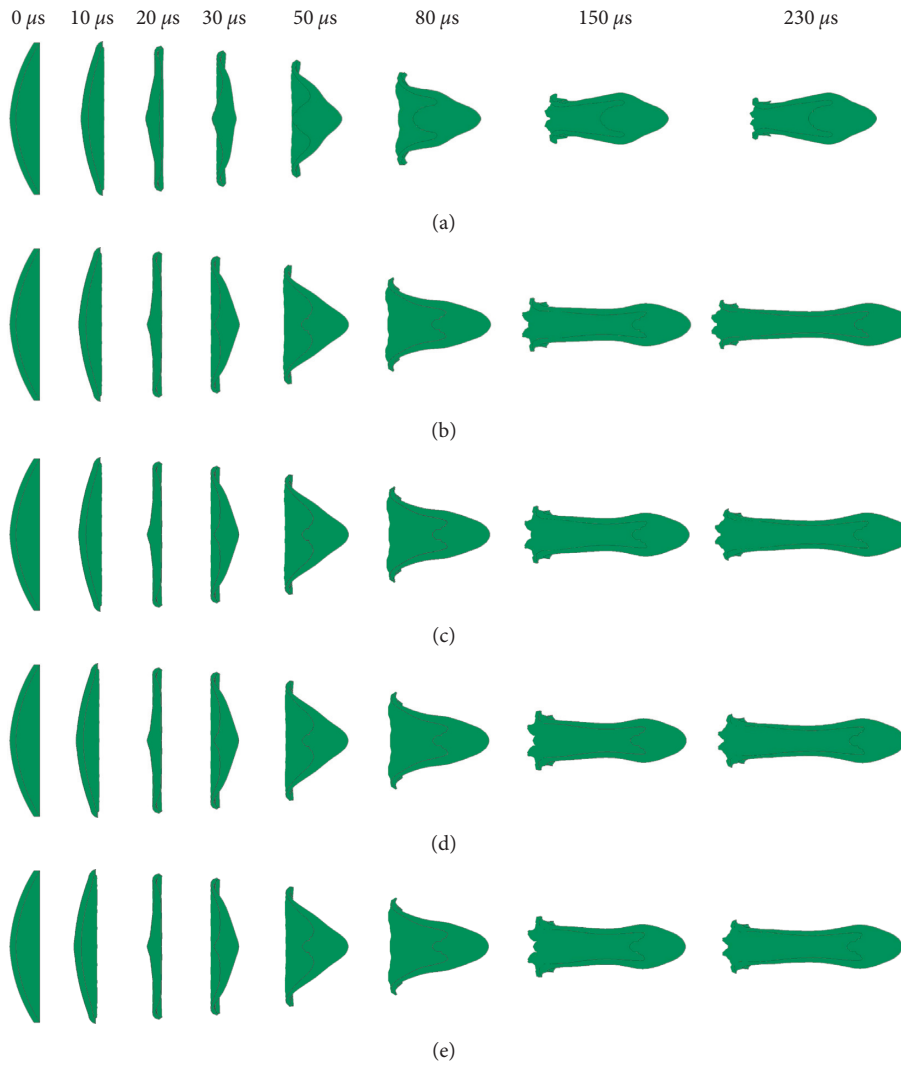


FIGURE 13: The forming shape of EFP under various deletion times after detonation. (a) $10 \mu\text{s}$ after detonation. (b) $20 \mu\text{s}$ after detonation. (c) $30 \mu\text{s}$ after detonation. (d) $50 \mu\text{s}$ after detonation. (e) $80 \mu\text{s}$ after detonation.

5.1. *Effect of Action Time on EFP Forming Shape.* To study the effect of detonation product time on EFP forming, the ALE unit deletion time of the explosive and air was set to 10, 15,

20, 30, 50, 80, and $100 \mu\text{s}$. The forming shape of EFP, and the change curve of relevant parameters under various working conditions is shown in Figures 13 and 14.

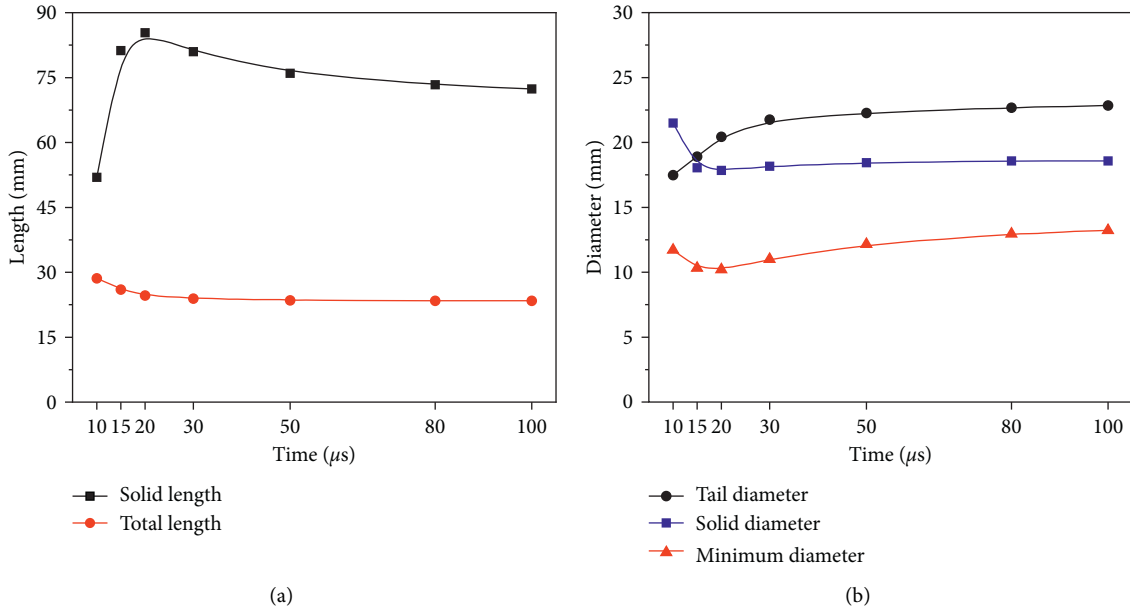


FIGURE 14: Variation curve of shape characteristic parameters of EFP. (a) Length and length of compaction part. (b) Tail skirt, dense part, and minimum diameter.

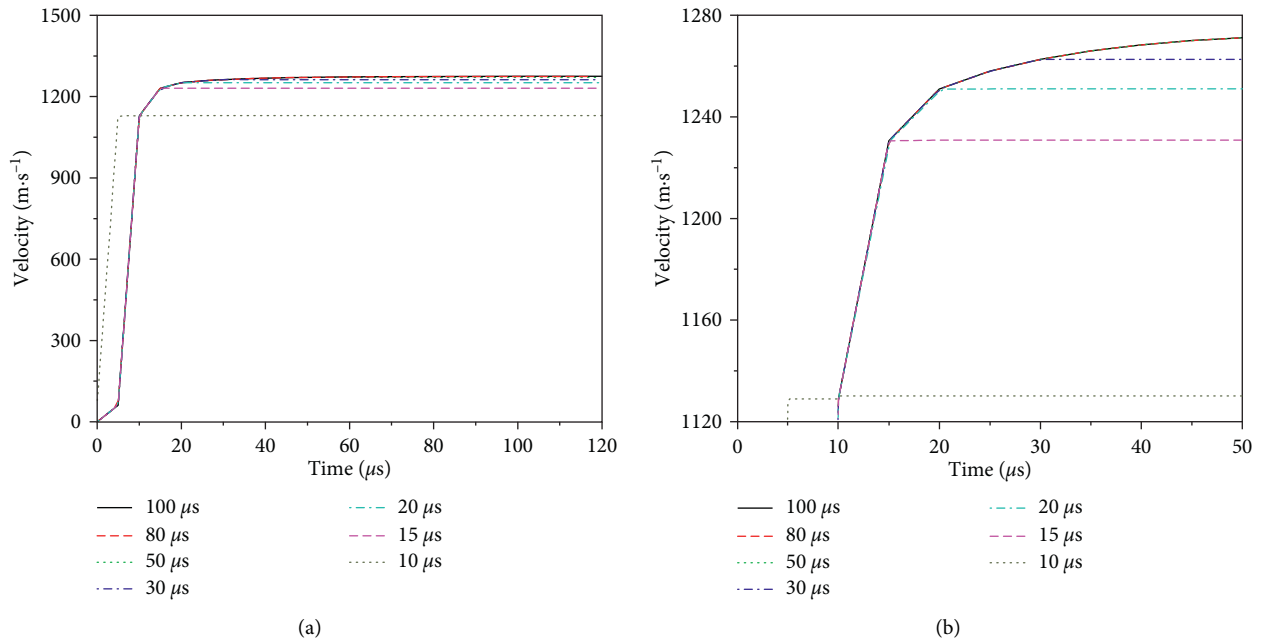


FIGURE 15: Velocity curve of EFP forming tip and tail. (a) Overall change curve. (b) Local magnification curve.

As shown in Figures 13 and 14, with a delay in deletion time, the morphological characteristic parameters of the EFP molding tended to be consistent. The shape of the EFP compact part was the fastest to stability, and the influence of the explosive and detonation products on its forming state after 30 μs could be neglected. However, the length and minimum diameter of EFP did not tend to stability until 80 μs. The length increased and then decreased, and the minimum diameter decreased and then increased.

5.2. Effect of Action Time on EFP Forming Velocity. Accordingly, the average velocity curve of the EFP under each working condition is shown in Figure 15.

As shown in Figure 15, with a delay in deletion time, the average velocity increased gradually and tended to be consistent. If ALE units, such as explosives and air, were deleted too early, the propelling effect of explosives and detonation products was not reflected fully, so the EFP velocity was lower than the actual situation. At 50 μs after

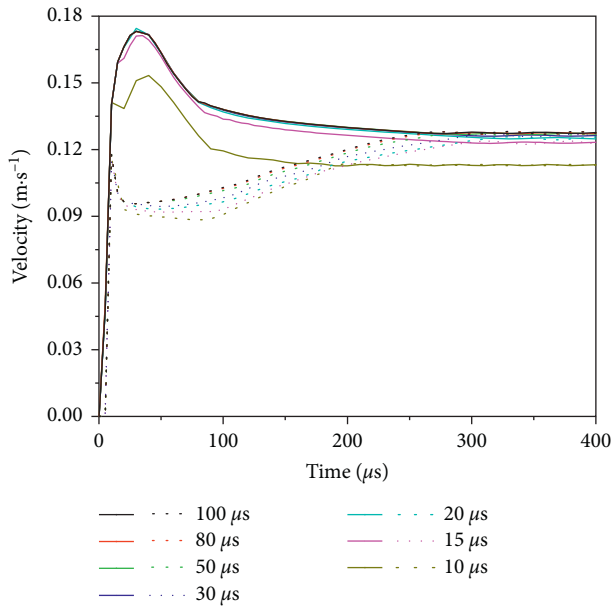


FIGURE 16: Velocity curve of EFP forming tip and tail.

charge initiation, the velocity of the tip of the EFP was hardly affected by the detonation products, but the detonation products still affected the EFP tail. The average velocity of the EFP was not affected after deleting units at $50 \mu\text{s}$. To further analyze the results, the velocity of the tip and tail change curve for EFP forming under various working conditions was obtained, as shown in Figure 16.

As shown in Figure 16, with a delay of deletion time, the gradual tip and tail velocity change tended to be the same, but the time for the tip and tail velocity to reach stability was not the same. The effect of detonation products on the velocity of EFP was reflected mainly in the tail velocity of the EFP. The velocity of the EFP tip was unaffected by the detonation products $30 \mu\text{s}$ after charge initiation, but the detonation products still affected the EFP tail. The influence of explosives and detonation products on EFP forming could be ignored $80 \mu\text{s}$ after the charge detonated.

In summary, when the calculation reached $80 \mu\text{s}$, the ALE elements, such as explosive and air, can be deleted, and the EFP Lagrange elements can be retained. The calculation could be continued to $400 \mu\text{s}$ or until the EFP was stable after a full restart. At this time, the calculation results remained valid, but the calculation time was reduced significantly.

6. Conclusions

In this work, the numerical simulation method of tantalum EFP forming has been established to analyze the influence of mesh size on tantalum EFP forming, compare the accuracy of JC constitutive parameters in different literature on the characterization of tantalum EFP forming, calculate the effective action time of detonation that drives EFP formation, and carry out experimental verification. The following conclusions can be drawn from the study presented in this article:

- (1) The EFP forming velocity was less sensitive to grid size. However, the EFP shape was highly sensitive to

grid size, and a large mesh size led to serious EFP shape distortion. The influence of air grid on EFP shape was less than that of the liner and charge, and the liner had the greatest influence. The air grid was divided into gradients, and the size increased gradually, which improved the computational efficiency.

- (2) For the same density and different constitutive parameters, the velocity of the stabilized EFP was the same, but the change trend of velocity was different, which led to the difference in morphology. A different stress-strain relationship led to a different liner action under the action of explosive and detonation products and formed different EFP shapes. The final stable velocity of the EFP was unaffected by the material stress-strain relationship, but depended on the material density or liner quality. The verification test showed that a selection of appropriate JC constitutive parameters could simulate tantalum EFP forming. Based on a comprehensive consideration, the parameters in constitutive of 7 and 9 are recommended.
- (3) The effect of detonation products on EFP forming was reflected mainly in the axial acceleration and radial contraction of the tail skirt. The velocity of the EFP tip was unaffected by the detonation products $30 \mu\text{s}$ after the charge initiations, but the detonation products still affected the EFP tail. The influence of explosives and detonation products on EFP forming can be ignored $80 \mu\text{s}$ after the charge detonates. At this time, ALE elements, such as explosive and air, can be deleted, and the Lagrange element of the EFP (liner) can be retained. A full restart can be used to continue the calculation until EFP forming is stable, to improve the calculation efficiency.

The work done here shows that 3D ALE models can be used with overall excellent results and low computational effort to reproduce the formation of tantalum EFP, which provides guidance for the design and engineering application of tantalum EFP. In order to further discuss the full process of a tantalum EFP, however, the work still needs to be done in penetration/perforation and postimpact process at subsequent research studies.

Data Availability

The data that support the findings of this study are available from the corresponding author upon reasonable request.

Conflicts of Interest

The authors declare that they have no conflicts of interest.

Acknowledgments

This work was financially supported by the National Natural Science Foundation of China (Grant no. 11202103).

References

- [1] M. F. Rasheed, C. Wu, and A. Raza, "Effect of explosive reactive armour cover plate on interaction of ERA and explosively formed projectile," *Shock and Vibration*, vol. 2019, Article ID 6093621, 10 pages, 2019.
- [2] F. Rondot, "Terminal ballistics of EFPs—a numerical comparative study between hollow and solid simulants," in *Proceedings of the 19th International Symposium on Ballistics*, pp. 1455–1461, Interlaken, Switzerland, 2001.
- [3] R. Fong and J. Kraft, "Advances in non-tantalum EFP warhead designs," in *Proceedings of the 21th International Symposium on Ballistics*, pp. 721–727, Adelaide, South Australia, 2004.
- [4] R. Castedo, A. P. Santos, J. I. Yenes, J. A. Sanchidrian, L. M. Lopez, and P. Segarra, "Finite elements simulation of improvised explosively formed projectiles," *Engineering Computations*, vol. 35, no. 8, pp. 2844–2859, 2018.
- [5] G. R. Johnson and R. A. Stryk, "Some considerations for 3D EFP computations," *International Journal of Impact Engineering*, vol. 32, no. 10, pp. 1621–1634, 2006.
- [6] D. Cardoso and F. Teixeira-Dias, "Modelling the formation of explosively formed projectiles (EFP)," *International Journal of Impact Engineering*, vol. 93, no. 7, pp. 116–127, 2016.
- [7] P. Mulligan and M. R. Jensen, "Numerical modelling of explosively formed projectiles compared with experiments and results of a numerical sensitivity study," *International Journal of Vehicle Performance*, vol. 1, no. 1, pp. 1–350, 2022.
- [8] Z. Zhang and W. W. Jin, "Finite element modeling of the shaped charge jet and design of the reusable perforating gun," *Petroleum Science*, vol. 17, no. 5, pp. 1389–1399, 2020.
- [9] A. Wojewódka and T. Witkowski, "Methodology for simulation of the jet formation process in an elongated shaped charge," *Combustion, Explosion and Shock Waves*, vol. 50, no. 3, pp. 362–367, 2014.
- [10] S. Pappu and L. E. Murr, "Hydrocode and microstructural analysis of explosively formed penetrators," *Journal of Materials Science*, vol. 37, no. 2, pp. 233–248, 2002.
- [11] A. P. Baêta-Neves and A. Ferreira, "Shaped charge simulation using SPH in cylindrical coordinates," *Engineering Computations*, vol. 32, no. 2, pp. 370–386, 2015.
- [12] G. R. Johnson and W. H. Cook, "A constitutive model and data for metals subjected to large strains high strain rates and high temperatures," in *Proceedings of the 7th International Symposium on Ballistics*, pp. 541–547, Netherlands, 1983.
- [13] D. J. Steinberg and C. M. Lund, "A constitutive model for strain rates from 10^{-4} to 10^6 s^{-1} ," *Journal of Applied Physics*, vol. 65, no. 4, pp. 1528–1533, 1989.
- [14] F. J. Zerilli and R. W. Armstrong, "Description of tantalum deformation behavior by dislocation mechanics based constitutive relations," *Journal of Applied Physics*, vol. 68, no. 4, pp. 1580–1591, 1990.
- [15] S. R. Chen and G. T. Gray, "Constitutive behavior of tantalum and tantalum-tungsten alloys," *Metallurgical and Materials Transactions A*, vol. 27, no. 10, pp. 2994–3006, 1996.
- [16] J. B. Kim and H. Shin, "Comparison of plasticity models for tantalum and a modification of the PTW model for wide ranges of strain, strain rate, and temperature," *International Journal of Impact Engineering*, vol. 36, no. 5, pp. 746–753, 2009.
- [17] J. X. Peng, Y. L. Li, and D. H. Li, "An experimental study on the dynamic constitutive relation of tantalum," *Explosion and Shock Waves*, vol. 23, no. 2, pp. 183–187, 2003.
- [18] B. L. Yang, D. J. Zhang, L. Q. Ji, J. Luo, H. Zhen, and Y. H. Ning, "Application of pure tantalum constitutive relation in EFP," in *Proceedings of the 14th National Symposium on Warhead and Damage Technology*, pp. 1248–1252, Chongqing, China, 2015.
- [19] Y. J. Wang, W. B. Li, W. B. Li, and X. T. Zhu, "The characteristics of forged tantalum and dynamic constitutive modelling," *Rare Metal Materials and Engineering*, vol. 36, no. 1, pp. 23–27, 2007.
- [20] Y. J. Wang, W. B. Li, and W. B. Li, "Mechanical Properties and Constitutive Relationship of High Purity Tantalum at High Temperature and High Strain Rate," in *Proceedings of the 11th Seminar on Experimental Technology of Explosive Mechanics*, Nanjing, China, 2020.
- [21] Y. J. Wang, W. B. Li, W. B. Li, and X. Wang, "Influence of structural characteristics on EFP formation under different liner materials," in *Proceedings of the 31st International Symposium on Ballistics*, pp. 2094–2105, DEStech Publications, Lancaster, UK, 2019.
- [22] T. F. Guo, W. B. Li, W. B. Li, and X. Hong, "Controlling effect of tantalum liner's structural parameters on EFP formation and penetration performance," *Chinese Journal of High Pressure Physics*, vol. 32, no. 03, pp. 96–103, 2018.
- [23] Z. P. Zhu, J. B. Men, J. W. Jiang, and W. Shuyou, "Forming control of tantalum EFP with large aspect ratio," *Acta Armamentarii*, vol. 39, no. S1, pp. 29–36, 2018.
- [24] W. B. Li, X. L. Dong, X. J. Shen, S. Ping, and X. Wen-Xu, "Simulation study on EFP with stable tail fins formed by polygonal shaped charge liner," in *Proceedings of the 31st International Symposium on Ballistics*, MDPI, Switzerland, 2019.
- [25] M. Kumar, Y. Singh, and P. Kumar, "Effect of detonation wave profile on formation of explosively formed projectile (EFP)," in *Proceedings of the 31st International Symposium on Ballistics*, pp. 1909–1915, DEStech Publications, Lancaster, UK, 2019.
- [26] L. Ding, J. W. Jiang, S. Y. Wang, and L. Q. Ji, "Tantalum EFP's forming and fracture characteristics," *Acta Armamentarii*, vol. 42, no. S1, pp. 53–58, 2021.
- [27] R. Li, W. B. Li, H. Z. Jin, and W. Guilin, "Theoretical analysis about interaction parameters of detonation waves based on jones-wilkins-lee equation of state," *Acta Armamentarii*, vol. 40, no. 3, pp. 516–521, 2019.
- [28] Group Gmx-6, "Selected hugoniots," in *Technical Report No. LA-4167-MSUS*: Los Alamos National Laboratory, Los Alamos, NM, 1969.
- [29] H. B. Ma, Y. F. Zheng, H. F. Wang, C. Ge, and Ch Su, "Formation and impact-induced separation of tandem EFPs," *Defence Technology*, vol. 16, no. 3, pp. 668–677, 2020.